JOURNAL OF GEOPHYSICAL RESEARCH, VOL. 108, NO. C5, 3139, doi:10.1029/2001JC001287, 2003

Effects of wave-current interaction on shear instabilities of longshore currents

H. Tuba Özkan-Haller
College of Oceanic and Atmospheric Sciences, Oregon State University, Corvallis, Oregon, USA

Ye Li
Department of Naval Architecture and Marine Engineering, University of Michigan, Ann Arbor, Michigan, USA

Received 4 January 2002; revised 11 June 2002; accepted 2 October 2002; published 3 May 2003.

[1] We examine the effects of wave-current interaction on the dynamics of instabilities of the surf zone longshore current. We utilize coupled models for the simulation of the incident waves and the wave-induced nearshore circulation. The coupling between the models occurs through radiation stress gradient terms (accounting for the generation of nearshore circulation) and through wave-current interaction terms (leading to the modification of the wave field by the generated circulation field). Simulations are carried out with a realistic barred beach configuration and obliquely incident waves for two frictional regimes. The results show that the shear instabilities of the longshore current have a significantly altered finite amplitude behavior when wave-current interaction effects are included for beaches with relatively high frictional damping. The primary effects are a reduction of the offshore extent of the motions and a delay of the onset of instabilities. In addition, the energy content of the motions within two surf zone widths is reduced, the propagation speed increases, and tendency to form offshore directed jets is reduced. The horizontal mixing induced by the instabilities is also reduced when wave-current interaction is considered, leading to a larger peak mean longshore current and a larger offshore current shear. These effects appear to be primarily linked to a feedback mechanism, whereby the incident wave field gains energy at locations of offshore directed currents. For more energetic shear instability fields that occur when frictional damping is small, this feedback affects the propagation speed and energy content of the instabilities near and onshore of the current peak only minimally. However, the offshore extent of the motions and the tendency to shed vortices offshore are still reduced. A reduction in the mixing due to the instabilities is evident offshore of the current peak, hence the mean longshore current profile is only affected offshore of the current peak. The inclusion of wave-current interaction significantly affects the shear instability signature observed in the shoreline runup for either frictional regime. These results indicate that the energy content and frequency extent of the shoreline response is increased markedly due to the wave-current interaction process. This effect appears to be related to variations in the forcing of the circulation that arise due to the refraction of the incident waves around offshore directed features of the circulation. *INDEX TERMS:* 4255 Oceanography: General: Numerical modeling; 4512 Oceanography: Physical: Currents; 4546 Oceanography: Physical: Nearshore processes; *KEYWORDS:* hydrodynamic instability, longshore currents, surf zone circulation, wave-current interactions

Citation: Özkan-Haller, H. T., and Y. Li, Effects of wave-current interaction on shear instabilities of longshore currents, *J. Geophys. Res.*, *108*(C5), 3139, doi:10.1029/2001JC001287, 2003.

1. Introduction

[2] Coherent long period undulations of the wave-induced surf zone longshore current were first observed by *Oltman-Shay et al.* [1989]. It is now widely believed that these undulations result from a shear instability of the longshore current. This mechanism has since been the subject of a number of numerical and physical experimental studies (for a review see *Dodd et al.* [2000]). The sum of these results shows that the surf zone longshore current can develop undulations due to an instability mechanism for a relatively wide range of bathymetries and forcing conditions. Numerical studies show that the velocity fluctuations occur in both the longshore and cross-shore velocity components over timescales of O(100–1000 s) and can reach magnitudes of 0.5 m/s for cases that involve a mean longshore current peak of 1 m/s. The resulting disturbances

0148-0227/03/2001JC001287$09.00

propagate alongshore at a fraction of the peak mean longshore current velocity and are nearly nondispersive. All of these results are in agreement with field observations. Computational studies also show that the character of the flow is a strong function of the amount of dissipation present at a given beach, ranging from low-energy equilibrated shear waves to highly energetic flow regimes reminiscent of a turbulent shear flow [*Slinn et al.*, 1998]. The particular data-model comparison of *Özkan-Haller and Kirby* [1999] suggests that the early observations of *Oltman-Shay et al.* [1989] were the result of a highly energetic shear instability field and are, therefore, representative of one extreme of the range of possible regimes.

[3] Model simulations of energetic shear instability regimes often also involve localized, strong, offshore directed jets. Since angles of wave incidence in shallow water are typically small, ambient offshore directed currents can significantly alter the incident wave field through current-induced refraction, diffraction, and shoaling processes; if an opposing current is strong enough, current-induced breaking will occur. In situations where the wave field is strongly altered by the nearshore flows, a feedback mechanism may be established since significant changes in the wave field will, in turn, alter the nature of the forcing of the nearshore circulation. Several recent numerical model studies suggest that such a feedback mechanism is significant for the dynamics of rip currents [*Haas et al.*, 1999; *Yu and Slinn*, 2003], but the effect on the dynamics of shear instabilities is unknown.

[4] Modeling the possible feedback between the wave field and the generated circulation field can be accomplished in several ways. One approach is to utilize a nonlinear phase-resolving wave model that possesses the physics that will lead to the generation of wave-induced currents, such as a model based on the Boussinesq equations [e.g., *Madsen et al.*, 1997; *Chen et al.*, 1999]. In these models, the feedback between the waves and currents is implicitly included. Another approach involves the artificial separation of the wave and current motions and the utilization of separate models to simulate their respective evolution. The coupling between the wave and circulation models occurs through radiation stress gradient terms (accounting for the wave momentum that results in the generation of currents) and through wave-current interaction terms (leading to the modification of the wave field by the generated circulation field in a feedback loop).

[5] Due to reasons related to computational efficiency, the second approach has traditionally been more popular. A recent example is the model used by *Haas et al.* [1999], who simulated the feedback between the incident waves and the circulation field in a rip current system by using a time-dependent circulation model coupled with a steady state wave model. Steady wave models explicitly assume that neither the wave energy incident on the beach nor the ambient current field (in this case, the generated circulation field) vary in time. The first assumption limits the applicability of such models to conditions where the wave field is stationary and no wave grouping exists. The second assumption limits the applicability of the overall model to situations where the current velocities are constant. In situations where the current velocities vary in time, such models are applied with the assumption that the wave field adjusts instantaneously to any variations in the circulation field. In this case, the wave field can be updated periodically using a snapshot of the circulation field. This assumption is reasonable when ambient currents vary slowly in time compared to the period of the incident waves. However, studies of finite amplitude shear instabilities have shown that currents in the surf zone can vary relatively rapidly (by $\sim$1 m/s over $\sim$5 wave periods), especially in the vicinity of vortex structures [see *Slinn et al.*, 1998; *Özkan-Haller and Kirby*, 1999]. In such situations an approach involving a steady wave model may be inadequate and the explicit modeling of a nonstationary wave field may become important. Such a wave model can also remedy other shortcomings of the abovementioned approach, since situations where the offshore wave height changes slowly due to an approaching storm or where wave grouping is pronounced can also be addressed.

[6] A model that explicitly accounts for temporal variations of the phase-averaged properties of the wave field was developed by *Yoo and O'Conner* [1988]. Their model is based on linear water wave theory and uses the energy equation for the incident waves to model the dynamics of the wave field, coupled with the conservation of wavenumber principle that can account for effects of wave refraction and diffraction. *Yoo and O'Conner* [1988] applied their model to situations that did not involve an underlying current. Instead, temporal changes in the wave field were induced due to changes in the bottom bathymetry. *Park and Borthwick* [2001] more recently extended the model of *Yoo and O'Conner* [1988] to include the effects of a variable current in the framework of a quadtree grid numerical model. They successfully applied the scheme to the simulation of the circulation on an idealized laboratory beach with sinusoidally varying bottom contours. Although their model equations are formulated such that they allow for the existence of a time-dependent wave and current field, their study only examined cases where steady-state solutions were being sought.

[7] In this study, we specifically examine a case where phase-averaged properties of the wave field are expected to vary temporally due to the existence of a time-dependent circulation field. In order to address this situation, we utilize a circulation model based on the depth- and time-averaged Navier Stokes equations along with a wave model based on a simplified version of the model presented by *Park and Borthwick* [2001]. We discuss our model equations in detail in section 2.

[8] Our goal is to isolate the effect of wave-current interaction on the evolution and dynamics of shear instabilities of the longshore current. We simulate the shear instability field for a realistic barred bottom bathymetry and incident wave field and compare the results while including or excluding wave-current interaction. We seek to identify the effects of wave-current interaction on several aspects of the instability and mean circulation field. In particular, we are interested in the impact of wave-current interaction on the general character of the instabilities, the energetics and alongshore propagation speed of the resulting motions, the mean momentum balance in the nearshore, the resulting mean longshore current profile, and the signature of the instabilities in the shoreline runup. We present the results of

these inquiries in section 3 and discuss and summarize our findings in section 4.

2. Model Formulation

2.1. Circulation Model

[9] The depth-integrated time-averaged Navier Stokes equations dictate the time-dependent behavior of the water surface elevation and flow velocities averaged over the incident waves. The equations include the effects of unsteady forcing due to the radiation stress gradients induced by the incident waves. Also included are the effects of momentum dissipation and diffusion due to bottom friction and lateral momentum mixing, respectively.

$$\frac{\partial \eta}{\partial t}+\frac{\partial}{\partial x}[u(h+\eta)]+\frac{\partial}{\partial y}[v(h+\eta)]=0, \tag{1a}$$

$$\frac{\partial u}{\partial t}+u\frac{\partial u}{\partial x}+v\frac{\partial u}{\partial y}=-g\frac{\partial \eta}{\partial x}+\tilde{\tau}_x+\tau'_x-\tau_{bx}, \tag{1b}$$

$$\frac{\partial v}{\partial t}+u\frac{\partial v}{\partial x}+v\frac{\partial v}{\partial y}=-g\frac{\partial \eta}{\partial y}+\tilde{\tau}_y+\tau'_y-\tau_{by}. \tag{1c}$$

Here, η is the water surface elevation above the still water level, h is the depth with respect to the still water level, u and v are the depth-averaged current velocities in the x and y directions, respectively, where x points offshore and y points in the longshore direction. The parameters $\tilde{\tau}_x$ and $\tilde{\tau}_y$ represent the effect of the incident wave forcing and are modeled using the radiation stress forcing formulation of *Longuet-Higgins and Stewart* [1964].

$$\tilde{\tau}_x=-\frac{1}{\rho d}\left(\frac{\partial S_{xx}}{\partial x}+\frac{\partial S_{xy}}{\partial y}\right), \qquad \tilde{\tau}_y=-\frac{1}{\rho d}\left(\frac{\partial S_{xy}}{\partial x}+\frac{\partial S_{yy}}{\partial y}\right). \tag{2}$$

Here, $d = h + \eta$ is the total water depth. The parameters S_{xx}, S_{xy} and S_{yy} denote the components of the radiation stress tensor and are computed using linear water wave theory [see *Özkan-Haller and Kirby*, 1999].

[10] The parameters τ_{bx} and τ_{by} represent bottom friction. We utilize a linear dissipation term such that

$$\tau_{bx}=\frac{\mu}{d}u, \quad \tau_{by}=\frac{\mu}{d}v, \tag{3}$$

where $\mu = (2/\pi)c_f u_0$ and u_0 is the amplitude of the horizontal orbital velocity of the incident waves obtained using linear wave theory. The parameter c_f is a friction coefficient, and a high degree of uncertainty exists regarding the value and variability of this coefficient in the nearshore zone. We consider c_f to be a constant, but carry out simulations with several different values to isolate the behavior of the system as a function of the dissipative nature of the beach. For a discussion of the adequacy of this formulation for surf zone applications, the reader is referred to *Özkan-Haller and Kirby* [1999].

[11] The parameters τ'_x and τ'_y represent the effect of lateral momentum mixing. We utilize an eddy viscosity formulation to approximate mixing due to turbulence and the otherwise-neglected depth variation in the current velocities. Following *Battjes* [1975] the eddy viscosity coefficient ν is assumed to be variable in the cross-shore direction with

$$\nu = Md\left(\frac{\epsilon_b}{\rho}\right)^{1/3}, \tag{4}$$

where ϵ_b is the energy dissipation due to wave breaking (discussed further below), and M is a constant mixing coefficient. Only the most dominant mixing terms are included to reduce necessary computational time. These terms are discussed in detail by *Özkan-Haller and Kirby* [1999] and will, for brevity, not be repeated here. However, it is noted that the dependence of the flow features on horizontal mixing is not a main concern here and we only wish to include an amount of mixing that is in the correct order of magnitude. Therefore, we will only discuss simulations for a mixing coefficient M of 0.25.

[12] Since the movement of the mean water surface elevation is considered, the temporal variation of the shoreline needs to be addressed. We model the shoreline movement by considering the kinematic condition at the shoreline given by

$$\frac{\partial \zeta}{\partial t}=u-v\frac{\partial \zeta}{\partial y}, \tag{5}$$

along with the condition that the total water depth $d = h + \eta$ is zero at the shoreline. Here, $\zeta(y, t)$ is the horizontal excursion of the shoreline, and u and v are evaluated at the shoreline.

[13] We note here that our treatment of the runup is very rudimentary. In particular, we define the shoreline as the location where the total water depth vanishes and assume that the wave-averaged mass flux at this location is zero. In reality, *Brocchini and Peregrine* [1996] show that a consistent derivation of the shoreline boundary conditions associated with wave-averaged models involves the specification of a non-zero mass flux that is a function of the location at which the mean shoreline is defined. They show that the longshore component of the mass flux due to motions in the swash zone may affect a significant area of the domain seaward of the swash zone, though this mass flux is still an order of magnitude smaller than that associated with the surf zone longshore current.

[14] A further assumption that significantly impacts our results near the shoreline involves the use of linear water wave theory for the specification of the velocities associated with the incident wave field. Since water waves become highly nonlinear near the shoreline, this assumption precludes our ability to accurately predict the dynamic and kinematic properties of the incident waves there. However, since models based on linear water wave theory have been successful in accurately predicting the mean water surface elevation near the shoreline [see *Mei*, 1990] as well as time variations near the mean shoreline [*Nakamura and Dodd*, 1999], our results regarding the low-frequency movement of the shoreline should still be relevant.

[15] We utilize a moving curvilinear grid that follows the movement of the shoreline defined above. Hence, the grid points are not stationary in space and time. An open

boundary condition is employed at the offshore boundary, where incoming short and long waves can be specified, and outgoing long waves are absorbed. We assume periodicity in the alongshore direction.

[16] The above equations are solved to obtain u, v, η and ζ as a function of time at each grid location given an initial condition. All simulations shown here are initiated from rest. The spatial derivatives contained in the governing equations are computed using spectral collocation methods, and the time derivative is approximated using a third-order Adams-Bashforth finite difference scheme. For a detailed description of the boundary conditions and numerical methods employed to solve the above equations, the reader is referred to *Özkan-Haller and Kirby* [1997] where the application of the model to the generation of subharmonic edge waves is also documented. The solution to the above-mentioned equations was also utilized by *Özkan-Haller and Kirby* [1999] to examine the shear instability field during 3 days of the SUPERDUCK field experiment [*Oltman-Shay et al.*, 1989].

[17] It will prove beneficial to examine the mean longshore momentum balance to isolate mixing effects due to the simulated shear instabilities. This can be achieved by longshore- and time-averaging the longshore momentum equation (1c) resulting in the balance

$$\left\langle \overline{u \frac{\partial v}{\partial x}} \right\rangle + \left\langle \overline{\tau_{by}} \right\rangle - \left\langle \overline{\tau'_y} \right\rangle - \left\langle \overline{\tilde{\tau}_y} \right\rangle = 0. \tag{6}$$

In the above equation, angled brackets and overlines denote the longshore average and time average of a variable, respectively. The forcing represented by the last term in equation (6) is balanced by the effects of bottom friction (second term), momentum mixing due to turbulence (third term) as well as effects of horizontal momentum mixing induced by the fluctuating components of the velocity field due to the shear instabilities (first term).

2.2. Wave Model

[18] In this study, we are interested in the feedback between the incident wave field and the generated time-varying circulation field. The forcing of the circulation field by the incident waves is already accounted for in the momentum equations (1b) and (1c). However, we also need to assess the effects of the currents on the incident waves. In the presence of a temporally varying circulation field, the wave energy is expected to vary in time as well, even in situations where the offshore wave field does not display any variations (in the form of wave groups). We model this variation by assuming a narrow banded incident spectrum with Rayleigh-distributed wave heights and utilizing the time dependent energy equation for the incident waves [*Phillips*, 1982].

$$\frac{\partial E}{\partial t} + \frac{\partial\big(E\big(u' + c_g \cos\theta\big)\big)}{\partial x'} + \frac{\partial\big(E\big(v' + c_g \sin\theta\big)\big)}{\partial y'} + S_{xx}\frac{\partial u'}{\partial x'} + S_{xy}\left(\frac{\partial u'}{\partial y'} + \frac{\partial v'}{\partial x'}\right) + S_{yy}\frac{\partial v'}{\partial y'} = -\epsilon_b. \tag{7}$$

Here, the x' and y' denote right-handed coordinate axes for wave propagation with x' pointing onshore and y' pointing alongshore. Hence, $x' = L_x - x$ and $y' = L_y - y$, where L_x and L_y are the domain lengths in the x and y directions, respectively. The energy of the incident waves E is given by (1/8) $\rho g H_{rms}^2$, θ and c_g are the local angle of incidence (measured counterclockwise from the x'-axis) and group velocity relative to the current associated with the peak frequency, respectively. The group velocity $c_g = n\ (\sigma/k)$, where $\sigma = (\omega - k_x u' - k_y v')$ is the intrinsic wave frequency and

$$n = \frac{1}{2}\left[1 + \frac{2kd}{\sinh 2kd}\right], \tag{8}$$

where ω is the absolute wave frequency and k is the wavenumber. The variables u' and v' denote the cross-shore and longshore current components in the (x', y')-coordinate system and are given by $u' = -u$ and $v' = -v$. Note that the last three terms on the left-hand side of equation (7) represent the wave-current interaction effects. Depending on their sign, these terms allow for the loss of wave energy to the currents or, alternately, for the infusion of energy from the currents to the incident waves. The parameter ϵ_b represents the wave-averaged breaking dissipation and is modeled using the formulation of *Thornton and Guza* [1983] given by

$$\epsilon_b = \frac{3\sqrt{\pi}}{16}\frac{\rho g B^3 f_p}{\gamma^4 d^5} H_{rms}^7. \tag{9}$$

Here, f_p is the peak frequency of a narrow banded spectrum with assumed Rayleigh distributed wave heights. The coefficients used for the wave height transformation model are $B = 0.78$ and $\gamma = 0.45$.

[19] In the presence of a time-varying current field, kinematic properties of the incident wave field will also vary in time. We model the time variation of the wavenumber vector $\mathbf{k}$ associated with the peak frequency by using the conservation of waves equations for the x-component k_x (= k cos θ) and the y-component k_y (= k sin θ) given by

$$\frac{\partial k_x}{\partial t} + \frac{\partial \omega}{\partial x'} = 0, \quad \frac{\partial k_y}{\partial t} + \frac{\partial \omega}{\partial y'} = 0, \tag{10}$$

where $\omega = 2\pi/T = 2\pi f_p$ is the absolute radial wave frequency given by

$$\big(\omega - k_x u' - k_y v'\big)^2 = gk \tanh kd. \tag{11}$$

The initial condition for the wavenumber is computed using the refraction equation

$$\nabla' \times \mathbf{k} = 0 \tag{12}$$

for the given bathymetry. Here,

$$\nabla'() = \frac{\partial()}{\partial x'}\mathbf{i} + \frac{\partial()}{\partial y'}\mathbf{j} \tag{13}$$

is the horizontal gradient operator in the (x', y') coordinate system. Note that if equation (12) is initially satisfied, it will be satisfied throughout the simulation. This can be shown by analyzing $\nabla' \times$ equation (10), which yields

$$\nabla' \times \left(\frac{\partial \mathbf{k}}{\partial t} + \nabla' \omega \right) = 0. \tag{14}$$

Since, by definition, $\nabla' \times \nabla' \omega = 0$, this implies that

$$\frac{\partial}{\partial t} (\nabla' \times \mathbf{k}) = 0, \tag{15}$$

stating that $\nabla' \times \mathbf{k} = 0$ will hold throughout the simulation provided it holds initially. A useful review of the refraction model used herein is given by *Dean and Dalrymple* [1991], and the reader is referred to this reference for a more complete bibliography on the subject.

[20] The energy equations (7) and wavenumber equation (10) account for the shoaling of the incident waves due to the circulation field. They also account for the refraction of the incident wave crests around any local features of the circulation field, such as narrow offshore directed current jets. They do not account for diffraction effects. Note that equation (10) implies that any temporal variation in the wavenumber components necessitates a spatial variation in the absolute wave frequency. This is because the wave field is not assumed to adjust instantaneously to the circulation field and the effects of current accelerations are included. We discuss the ramifications of a spatially varying absolute frequency in Appendix A.

[21] The energy equation (7) is solved in time given an initial condition and an offshore boundary condition. Periodicity is assumed in the longshore direction. The simulations are initiated from rest, so the wave energy is initially zero. The wave height at the offshore boundary is ramped up over about 5 wave periods. After this initial period, the wave height at the offshore boundary remains constant. In parallel to the solution method used for the circulation model described above, the spatial derivatives in the energy equation are computed using spectral collocation schemes.

[22] The wavenumber equations (10) are solved in conjunction with the dispersion relationship (11). We specify the wavenumber at the offshore boundary and use periodicity in the alongshore direction. Theoretically, no boundary condition is necessary at the shoreline. However, in practice, the governing equations are singular at the shoreline boundary where the total water depth is zero. The wavelength at this location should also be zero, resulting in an infinite wavenumber. In order to avoid singular values, we specify the wavenumber at the shoreline to correspond to its value at a small water depth (0.0075 m) and do not allow it to vary in time. This small water depth results in a large value for k at the shoreline, but the value is nonetheless finite. We note here that our results are insensitive to the exact value of k at the shoreline as long as this value is larger than k at the neighboring point but remains finite. We utilize Fourier collocation to compute spatial derivatives in the longshore direction. However, in the cross-shore direction we utilize an upward differencing scheme, since the Chebyshev collocation scheme performs poorly when the differentiated function tends to infinity (or a very large value, as in our case). The upward differencing scheme also introduces some numerical dissipation that helps alleviate problems related to the over-specification of the problem due to the existence of an additional boundary condition for k at the shoreline. Note that no additional noise filtering technique is applied to the solution of the energy equation (7) and equation (10) in the cross-shore direction. The test cases documented in Appendix A show that the solution methods used herein are well behaved.

2.3. Model Applications

[23] Our simulations are carried out for a longshore-uniform barred bathymetry that is composed of a plane beach of slope m and a superimposed bar in the form of a normal distribution. The water depth h is therefore given by

$$h(x) = mx - (mx - d_c) \exp\left\{ -30 \frac{(x - x_c)^2}{x_c^2} \right\}, \tag{16}$$

where d_c is the water depth over the bar crest and x_c is the cross-shore location of the bar crest. We carry out simulations for $m = 0.025$, $d_c = 1.1$ m and $x_c = 100$ m. The offshore boundary of the modeling domain is at $x = L_x = 300$ m and the wave field is specified at this location with wave height $H_{rms} = 1$ m, period $T = 10$ s and wave incidence $\theta = -10°$. The longshore width L_y of the domain is chosen to be 1000 m. To ensure high accuracy, we utilize 128 collocation points in both the cross-shore and longshore directions. The resulting small physical grid size in the cross-shore direction necessitates a time step of 0.025 s.

[24] Since bottom friction is a source of high uncertainty, we carry out simulations for several bottom friction coefficients. *Özkan-Haller and Kirby* [1999] found that horizontal mixing due to turbulence or vertical variations of the currents also affected the flow, but to a lesser degree. In particular, the propagation speed is affected minimally and, although the general character of the flow is altered, the tendency to form localized offshore directed features is only a weak function of the horizontal mixing. In contrast, the existence of offshore directed features is strongly linked to the amount of bottom friction imposed on the system; hence we concentrate on carrying out simulations for different friction coefficients but hold the mixing coefficient M constant at 0.25.

[25] We solve the full system of equations given by equations (1), (5), (7), (10), and (11) for the unknowns, η, u, v, ζ, E, k_x, k_y, and ω when wave-current interaction is considered. In cases where we wish to ignore wave-current interaction, we neglect all terms in the energy equation (7) and the dispersion relationship (11) that involve the horizontal velocities $u'(= -u)$ and $v'(= -v)$.

3. Results

[26] We begin our simulations with an example where the longshore length scale of the domain L_y is restricted to 250 m and the number of collocation points in the alongshore direction is restricted to four. In this situation, shear instabilities are artificially suppressed and we can analyze the nature of the wave height decay, longshore current and wave-induced setup in the absence of instabilities. Wave-current interaction is neglected, and Figure 1 shows time series of H, u, v, η, ζ, k_x, k_y and ω at the bar crest for $c_f = 0.007$. As expected, the cross-shore balance is set up

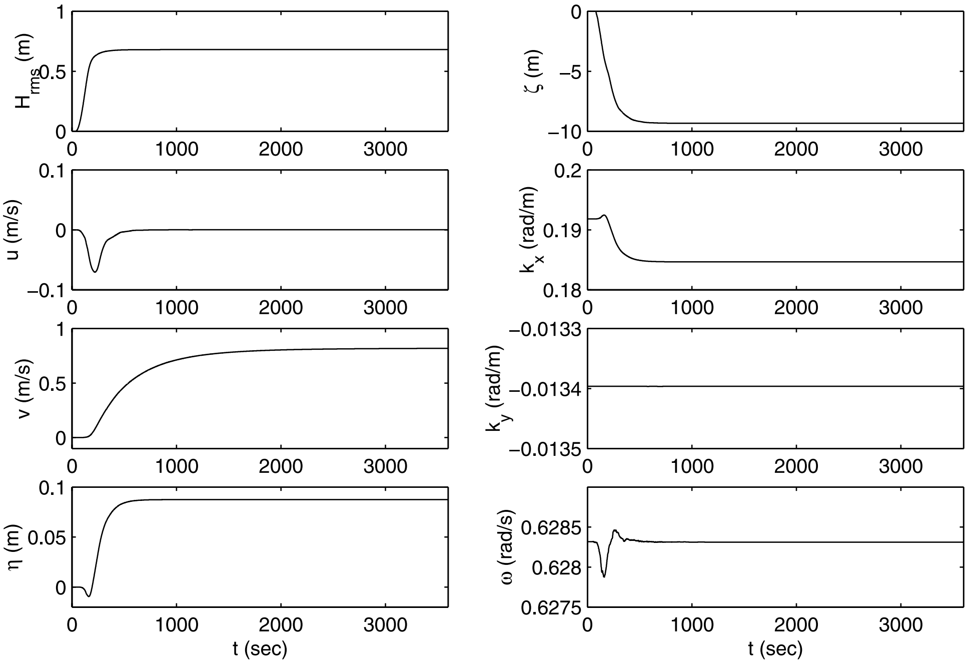

Figure 1. Time series of wave height H_{rms}, cross-shore velocity u, longshore velocity v, water surface elevation η, horizontal shoreline excursion ζ, cross-shore component of the wavenumber k_x, longshore component of the wavenumber k_y, and absolute frequency ω. Time series were sampled at $(x, y) = (100, 125)$ m except for ζ, which was sampled at $y = 125$ m. Offshore wave conditions at $x = 300$ m are: $H_{rms} = 1$ m, $\theta = -10°$, $T = 10$ sec.

quicker than the longshore balance; however, the longshore current is established within an hour. There is a variation in the wavenumber k_x in the first hour of simulation that corresponds to a lengthening of the waves from about 33 m wavelength to 34 m wavelength. This change is associated with the fact that the total water depth over the bar crest increases by about 10% due to the establishment of the wave-induced setup. An associated temporal change of small magnitude is also observed in the wave frequency. It should be noted that the cross-shore velocity and the frequency return to their original values once equilibrium is reached and a steady state solution is achieved. The resulting longshore current displays two distinct peaks due to the presence of two distinct areas of wave breaking over the bar crest and near the shoreline (see Figure 2). The inclusion of wave-current interaction has little effect on the results discussed above, since the component of the circulation along the propagation direction of the incident waves is weak at all times, even during the spin-up phase when a discernible cross-shore velocity component exists.

[27] Next, we utilize a longshore domain width L_y of 1000 m and carry out simulations for friction coefficients of $c_f = 0.007$ and 0.005 while including or excluding wave-current interaction. We will analyze the time-varying and mean properties of the motions separately below.

3.1. Time-Varying Motions

3.1.1. Results for $c_f = 0.007$

[28] Five-hour time series of the instability field in the absence of wave-current interaction for $c_f = 0.007$ are shown in Figure 3. The time series were collected at the cross-shore location of the bar crest ($x = 100$ m). We can observe that the instabilities are initiated within the first half hour of the simulation. The time series suggest relatively high-frequency oscillations at first (O(200 s) timescales); however, lower frequency oscillations become more prominent a few hours later (O(1000 s) timescales). This frequency downshifting is also typical of model simulations for measured bathymetry from Duck, N. C. [*Özkan-Haller and Kirby*, 1999]. The time series of the cross-shore wavenumber k_x displays a relatively large initial time variation as the setup is established. Subsequently, the wavenumber varies in response to small fluctuations in the water surface elevation. The time series of the surface elevation and cross-shore wavenumber are highly correlated and out of phase, implying a lengthening of the waves over deeper water. The variation of the wavenumber is small in magnitude and the net wavelength change is less than 1%. The associated temporal variation in the wave frequency corresponds to a change in the wave period of ±0.06% and is therefore negligible. The variation in the longshore wavenumber component is out of phase with the frequency and is also small in magnitude.

[29] When wave-current interaction is included, the instabilities require a longer period of time to reach finite amplitude (see Figure 4). Although the amplitude of the resulting longshore velocity fluctuations is comparable to those obtained in the absence of wave-current interaction, the amplitude of the cross-shore velocities is significantly reduced. The fluctuations appear to be more regular, since they are equilibrated with a period of ~600 s. The fluctuations in the cross-shore wavenumber are now much more pronounced (~19% variation in the wavelength) and are highly correlated and in phase with the cross-shore velocity

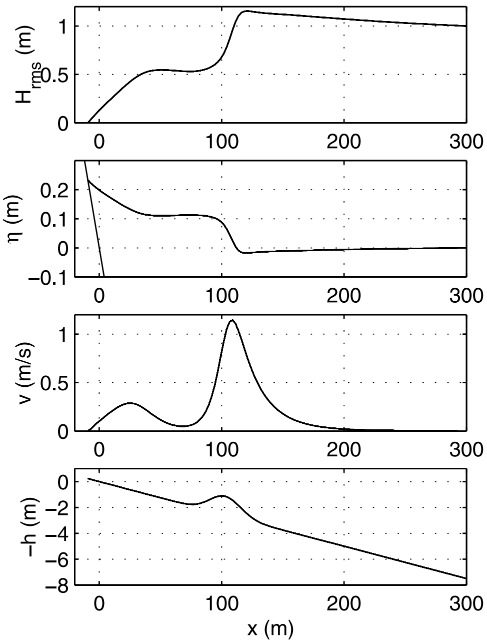

Figure 2. Cross-shore variation of wave height H_{rms}, water surface elevation η, longshore velocity *v*, and water depth *h* at $t = 3600$ s. Offshore wave conditions are stated in the caption of Figure 1.

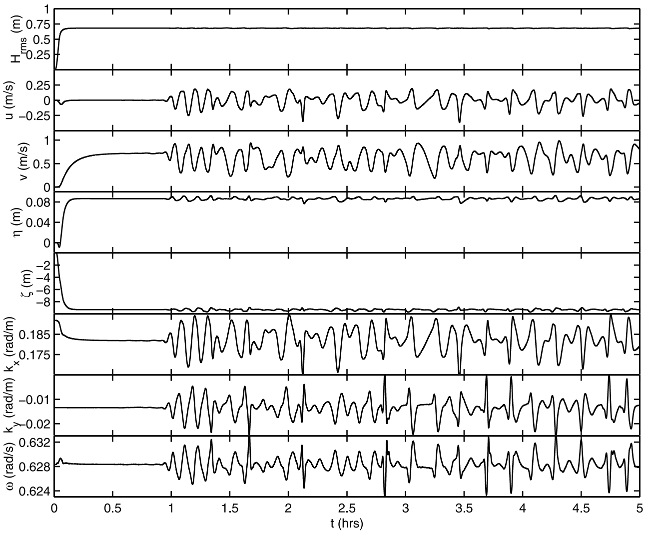

Figure 4. Time series for $c_f = 0.007$ including wave-current interaction. Results for wave height H_{rms}, cross-shore velocity *u*, longshore velocity *v*, water surface elevation η, horizontal shoreline excursion ζ, cross-shore component of the wavenumber k_x, longshore component of the wavenumber k_y, and absolute frequency ω are depicted. Time series were sampled at $(x, y) = (100, 500)$ m except for ζ, which was sampled at $y = 500$ m.

signal (correlation coefficient *r* of 0.96). Since the cross-shore velocity is positive when directed offshore, this implies that the waves shorten on an opposing current. The longshore wavenumber also varies significantly. The combined effect of the variations in the cross-shore and longshore wavenumber components result in a temporal variation of the wave angle by ∼±4° at this cross-shore location (where the local mean angle is ∼−4°). The longshore wavenumber time series and frequency time series are correlated ($r = 0.99$) and out of phase. Both time series are also significantly correlated with the acceleration associated with the cross-shore velocity ($r = 0.87$). The variation in the wave period due to the wave-current interaction process is ∼±1.75%.

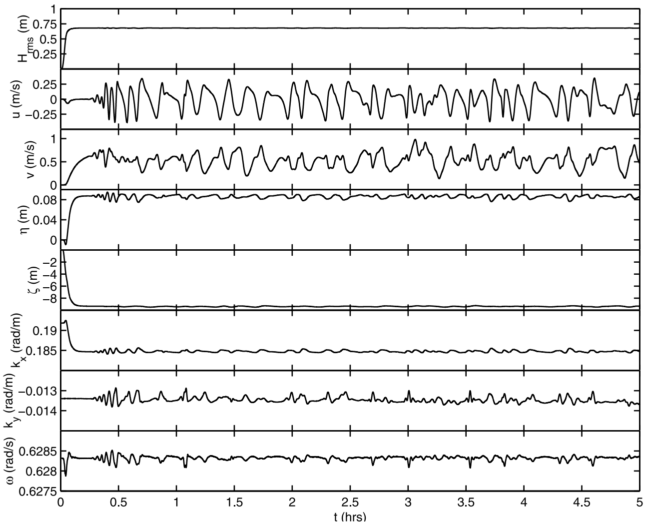

Figure 3. Time series for $c_f = 0.007$ neglecting wave-current interaction. Results for wave height H_{rms}, cross-shore velocity *u*, longshore velocity *v*, water surface elevation η, horizontal shoreline excursion ζ, cross-shore component of the wavenumber k_x, longshore component of the wavenumber k_y, and absolute frequency ω are depicted. Time series were sampled at $(x, y) = (100, 500)$ m except or ζ, which was sampled at $y = 500$ m.

[30] The spatial structure of the flow can be visualized utilizing snapshots of the vorticity *q* given by

$$q = \frac{\partial v}{\partial x} - \frac{\partial u}{\partial y}. \tag{17}$$

Snapshots of the vorticity field at $t = 4.2$ hours for cases neglecting and including wave-current interaction are shown in Figure 5. In both cases, the alternating regions of positive (yellow to red) and negative (blue) vorticity represent the two peaks of the longshore current profile. The vorticity around the bar crest displays a typical shear instability pattern when wave-current interaction is neglected. The current displays a significant meander that involves the occurrence of strong cross-shore currents in tandem with near-zero longshore current velocities, resulting in offshore directed currents that slowly propagate alongshore. The flow can be characterized as a nonlinear shear flow, but does not display the highly turbulent features that can be obtained on barred beaches for lower frictional damping [see *Slinn et al.*, 1998]. The cross-shore jets extend offshore about 200 m, which corresponds to about two surf zone widths.

[31] When wave-current interaction is included, the offshore extent of the flow features is drastically reduced. The vorticity around the bar crest displays variations with

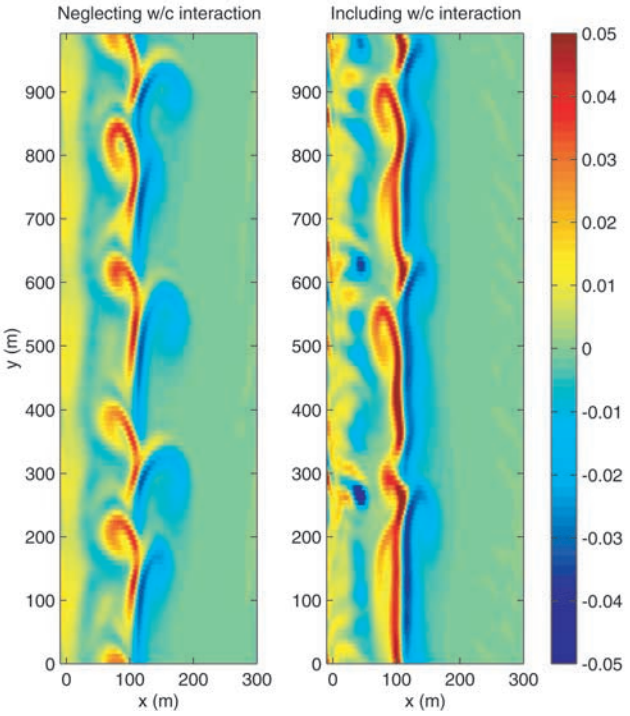

Figure 5. Snapshots of vorticity q (s^{-1}) at 4.2 hours for c_f = 0.007 (left) neglecting and (right) including wave-current interaction.

similar lengths scales as before; however, the offshore directed currents do not extend significantly offshore. Furthermore, there is noticeable activity in the shoreline jet, where vortex pairs appear to form. These vortices propagate alongshore, as will be shown next.

[32] Frequency-longshore wavenumber spectra can be utilized to obtain information about the propagation speed of the observed flow structures. These spectra are constructed using the last 8192 s of the computed time series at all longshore points at a given cross-shore location. A cosine taper is applied to the first and last 10% of the data and a two dimensional Fourier transform is used to construct the spectra. The resulting spectra are smoothed by averaging over eight frequencies and two wavenumbers. The spectra obtained using longshore velocities at three cross-shore locations are shown in Figures 6 and 7. Best fit dispersion lines have been obtained using a weighted first-order polynomial fit as described in *Özkan-Haller and Kirby* [1999] and the equations for these lines are noted above each plot.

[33] When wave-current interaction is neglected (Figure 6) the propagation speeds at different cross-shore locations show ~3% variations. The motions are most energetic near the bar crest (x = 100 m) but still display significant energy further offshore. When wave-current interaction is considered (Figure 7), the motions display a higher propagation speed by ~10%. The wavenumber extent of the spectra appears to be reduced slightly at the bar crest. The difference is most pronounced offshore of the bar crest, where the energy content and wavenumber extent of the motions is severely limited by wave-current interaction.

[34] In order to examine the nature of the motions near the shoreline that are especially apparent in the simulations including wave-current interaction, we examine the frequency-longshore wavenumber spectra of the horizontal shoreline runup estimates (Figure 8). We note that both the energy content and the frequency extent of the shoreline runup increases dramatically when wave-current interaction is taken into account.

3.1.2. Results for c_f = 0.005

[35] Time series of the instabilities computed while neglecting wave-current interaction for a lower frictional value of c_f = 0.005 (Figure 9) show amplitudes in both the cross-shore and longshore velocity signals that are higher than their higher friction counterparts. Also evident in the time series is an intermittent character that is evidenced by the existence of periods of time (from t = 2.5 to 3.5 hours) when oscillations with longer timescales (15 min) are dominant followed by periods of time (t > 4 hours) when oscillations with shorter timescales (5 min) are primarily observed. Such behavior was also observed by *Özkan-Haller and Kirby* [1999] in their simulations but was absent from the corresponding observations of *Oltman-Shay et al.* [1989].

[36] The variations in the cross-shore wavenumber k_x are once again small (<1%), as are variations in the absolute

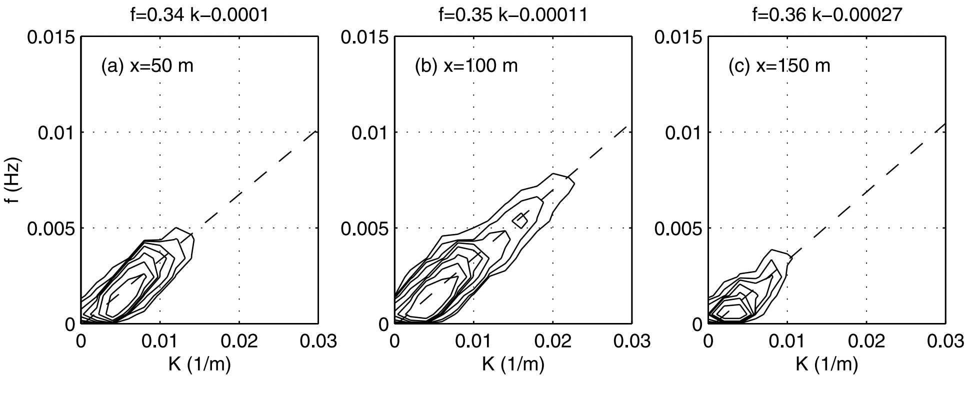

Figure 6. Frequency-longshore wavenumber spectra for c_f = 0.007 for longshore velocity computed while neglecting wave-current interaction at (a) x = 50 m, (b) x = 100 m, and (c) x = 150 m. Contour levels plotted are (10, 20, 40, 80, 160, 320, 640, 1280). The equation for the best-fit dispersion line (dashed line) is noted above each plot.

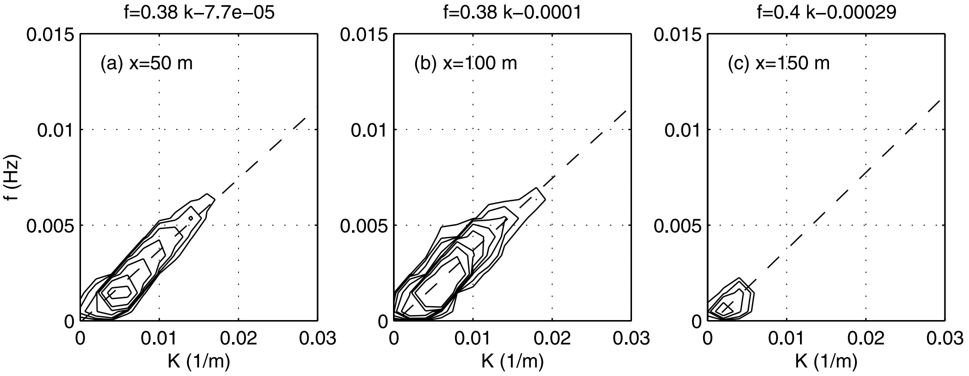

Figure 7. Frequency-longshore wavenumber spectra for $c_f = 0.007$ for longshore velocity computed while including wave-current interaction at (a) $x = 50$ m, (b) $x = 100$ m, and (c) $x = 150$ m. Contour levels plotted are (10, 20, 40, 80, 160, 320, 640, 1280). The equation for the best-fit dispersion line (dashed line) is noted above each plot.

frequency (<0.2%). Once again, the cross-shore wavenumber is out of phase with the water surface elevation signal. When wave-current interaction is considered (Figure 10) the time series no longer display an intermittent character. The variation in the cross-shore component of the wavenumber is in phase with the cross-shore velocity signal and the associated change in the wavelength can reach up to 25% of the mean wavelength. The absolute frequency changes appreciably and results in a change in wave period of 3%.

[37] Snapshots of the vorticity (Figure 11) show that the simulations neglecting wave-current interaction involve alongshore propagating features with wavelengths of about 200–300 m, although features with shorter length scales are at times observed as vortices collide and merge. Such flow characteristics were also described by *Özkan-Haller and Kirby* [1999]. The flow regime also involves the occasional occurrence of a vortex pair that is released a significant distance offshore. Several propagating features can be observed that involve strong and exclusively offshore directed jets. The offshore velocities at these locations exceed 0.5 m/s. The shoreline jet can be observed to be relatively inactive.

[38] In contrast, the shoreline jet appears to be much more active when wave-current interaction is considered. Vorticity fronts can be observed within the shoreline jet, and these fronts occasionally roll up and form vortex pairs. Over the bar crest, the flow features display somewhat longer length scales compared to the flow in the absence of wave-current interaction. Offshore propagating vortex pairs are absent altogether, and the offshore extent of the motions is significantly reduced, although some offshore directed flow features exist.

[39] While the increase in the propagation speed of the vorticity features was significant when wave-current interaction was considered for higher frictional values, the differences are less significant for this lower frictional value. A comparison between Figures 12 and 13 reveals that the propagation speeds of the motions are very similar in the presence or absence of wave-current interaction.

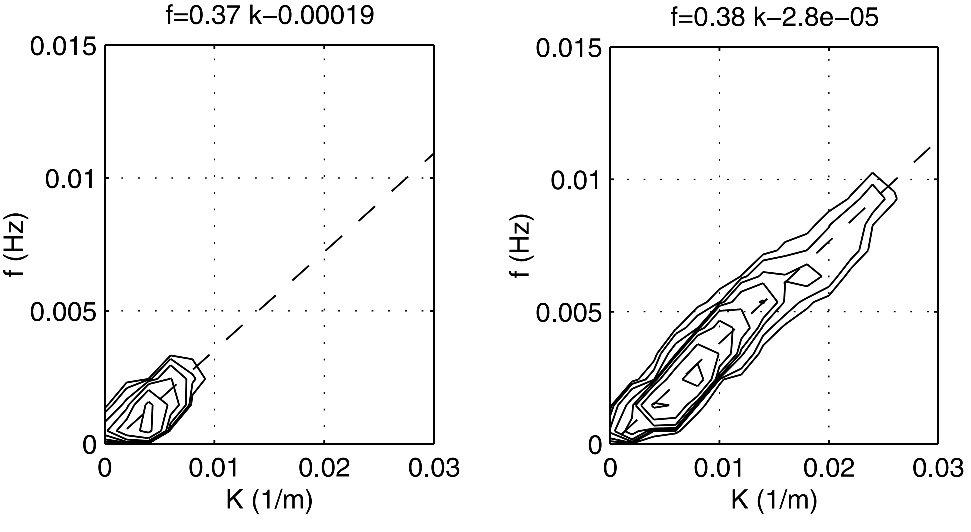

Figure 8. Frequency-longshore wavenumber spectra for $c_f = 0.007$ for shoreline runup computed while (left) neglecting and (right) including wave-current interaction. Contour levels plotted are (10, 20, 40, 80, 160, 320, 640, 1280). The equation for the best-fit dispersion line (dashed line) is noted above each plot.

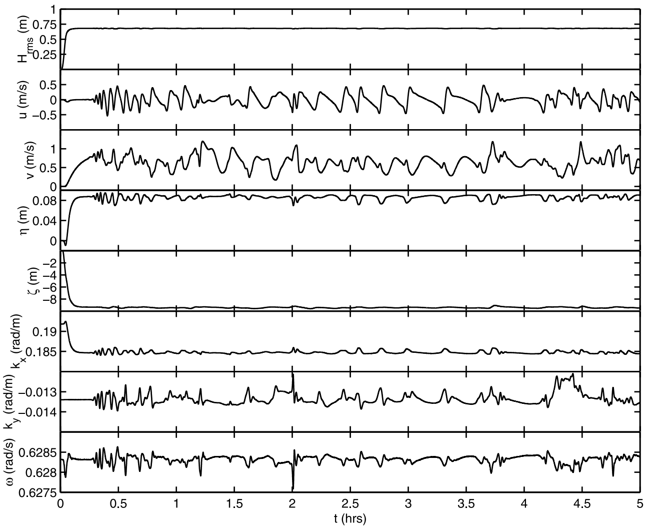

Figure 9. Time series for c_f = 0.005 neglecting wave-current interaction. Results for wave height H_{rms}, cross-shore velocity u, longshore velocity v, water surface elevation η, horizontal shoreline excursion ζ, cross-shore component of the wavenumber k_x, longshore component of the wavenumber k_y, and absolute frequency ω are depicted. Time series were sampled at (x, y) = (100, 500) m except for ζ, which was sampled at y = 500 m.

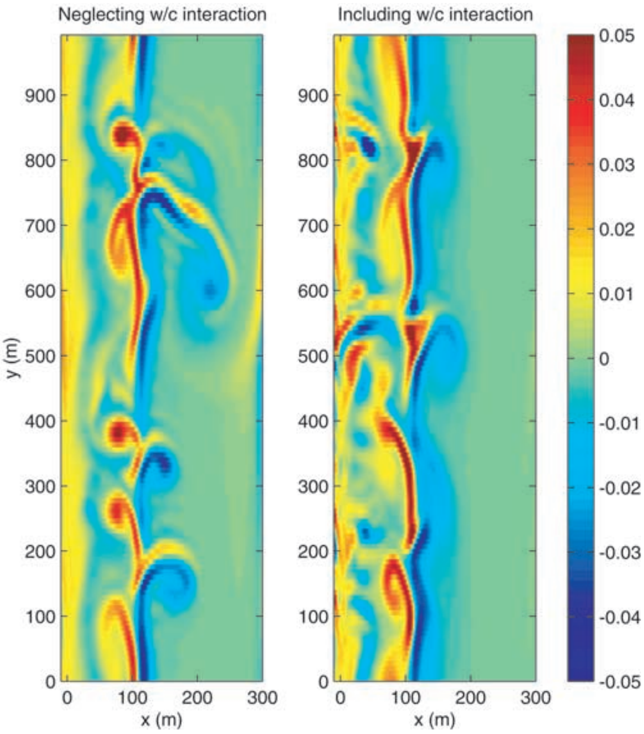

Figure 11. Snapshots of vorticity q (s^{-1}) at 4.6 hours for c_f = 0.005 (left) neglecting and (right) including wave-current interaction.

However, the energy content and frequency extent increase slightly in the bar trough region and decrease slightly offshore of the bar crest when wave-current interaction is considered. The most pronounced difference can be observed when examining the behavior of the shoreline jet. Figure 14 shows that, although the propagation speed of the motions has not changed significantly, the energy content and frequency extent has increased appreciably.

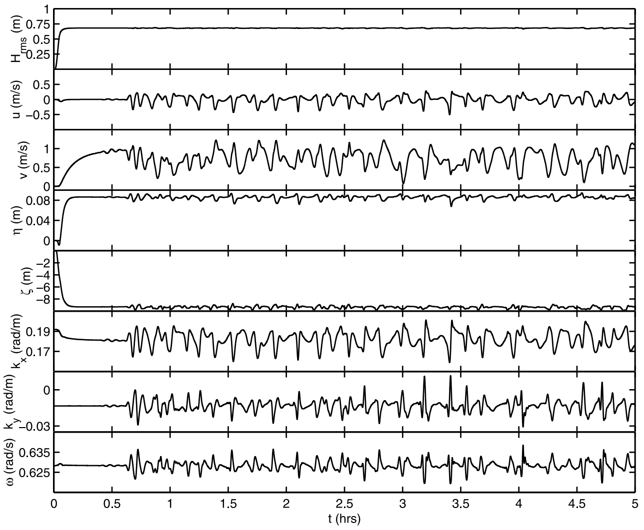

Figure 10. Time series for c_f = 0.005 including wave-current interaction. Results for wave height H_{rms}, cross-shore velocity u, longshore velocity v, water surface elevation η, horizontal shoreline excursion ζ, cross-shore component of the wavenumber k_x, longshore component of the wavenumber k_y, and absolute frequency ω are depicted. Time series were sampled at (x, y) = (100, 500) m except for ζ, which was sampled at y = 500 m.

3.2. Mean Quantities

[40] Longshore- and time-averaged mean longshore current profiles and turbulent kinetic energy estimates for c_f = 0.007 are shown in Figure 15. The longshore averages are performed over the entire width of the domain and the time averages are obtained using the last 8192 s of the time series. The turbulent kinetic energy is defined as

$$E'(x) = \frac{1}{2}\left\langle \overline{(u - \langle \bar{u} \rangle)^2} + \overline{(v - \langle \bar{v} \rangle)^2} \right\rangle \tag{18}$$

and provides a good measure of the cross-shore extent and distribution of the fluctuations due to the shear instabilities.

[41] The mean longshore current profile for c_f = 0.007 displays a maximum just offshore of the bar crest. A secondary maximum exists near the shoreline, but significant current velocities are also observed in the bar trough region. In the presence of wave-current interaction, the overall energy content of the instabilities is reduced; however, it is evident that the instabilities are more energetic in a narrow region near the shoreline. The reduction of the total offshore extent of the motions is quite evident. The longshore current associated with the simulation including the interaction terms displays a stronger peak and weaker currents in the bar trough region, indicating that less horizontal mixing is produced by the instabilities.

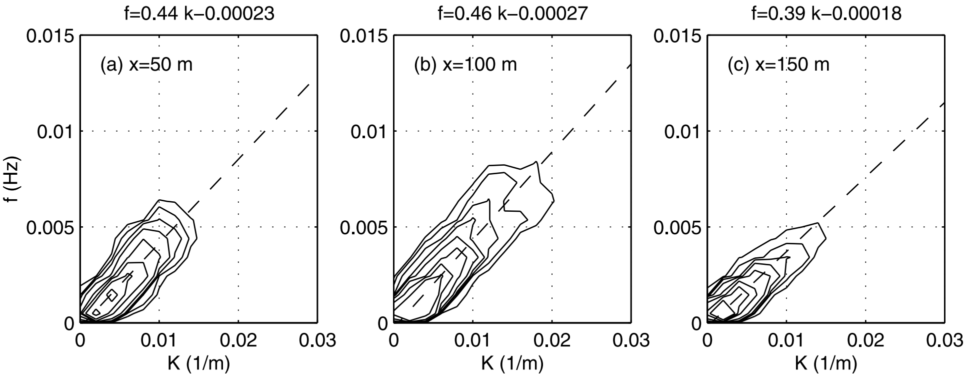

Figure 12. Frequency-longshore wavenumber spectra for $c_f = 0.005$ for longshore velocity computed while neglecting wave-current interaction at (a) x = 50 m, (b) x = 100 m, and (c) x = 150 m. Contour levels plotted are (10, 20, 40, 80, 160, 320, 640, 1280). The equation for the best-fit dispersion line (dashed line) is noted above each plot.

[42] The amount of mixing induced by the instabilities can be more accurately assessed with the help of the mean longshore momentum balance given by equation (6). In the absence of wave-current interaction, the mixing caused by the instabilities is the dominant mixing process (Figure 16). When wave-current interaction is considered the mean forcing of the longshore current is virtually identical to the case excluding the interaction terms; however, the shear instability response is such that significantly less lateral mixing is caused by the fluctuations.

[43] The longshore current profiles and turbulent kinetic energy estimates for c_f = 0.005 (Figure 17) also show differences between cases neglecting and including the interaction terms, but the differences are less pronounced, especially shoreward of the bar crest. The offshore extent of the motions is reduced when wave-current interaction is considered. The longshore current profiles show some differences near the current peak and farther offshore but almost no differences in the bar trough region or near the shoreline. The mean momentum balance (Figure 18) also confirms that the momentum mixing caused by the instabilities is similar, with less mixing predicted near and offshore of the current peak when wave-current interaction is considered.

4. Discussion and Conclusions

[44] As a result of our simulations, we find that wave-current interaction is important when frictional dissipation on a beach is moderately high and the flow is characterized by fluctuating eddies that cause offshore directed jets, but are generally confined to the longshore current and are not shed offshore. In these situations, wave-current interaction causes the onset of the instabilities to be delayed, and the tendency to form offshore directed jets to be reduced. The offshore extent and energy content of the shear instabilities are also reduced while their alongshore propagation speed increases when wave-current interaction is considered.

[45] In situations where the frictional damping is low and the flow is characterized by a turbulent shear flow that sheds vortex pairs offshore, wave-current interaction affects the propagation speed and frequency distribution of the energy over the bar crest only minimally. However, the offshore extent of the motions is reduced. The tendency of the flow

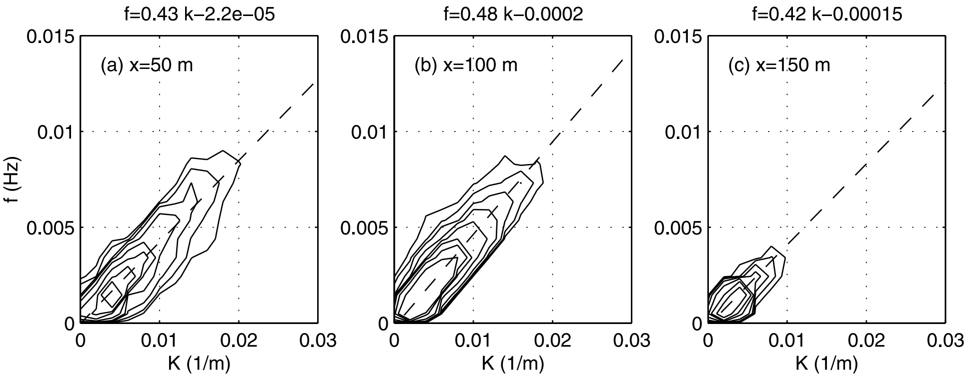

Figure 13. Frequency-longshore wavenumber spectra for $c_f = 0.005$ for longshore velocity computed while including wave-current interaction at (a) x = 50 m, (b) x = 100 m, and (c) x = 150 m. Contour levels plotted are (10, 20, 40, 80, 160, 320, 640, 1280). The equation for the best-fit dispersion line (dashed line) is noted above each plot.

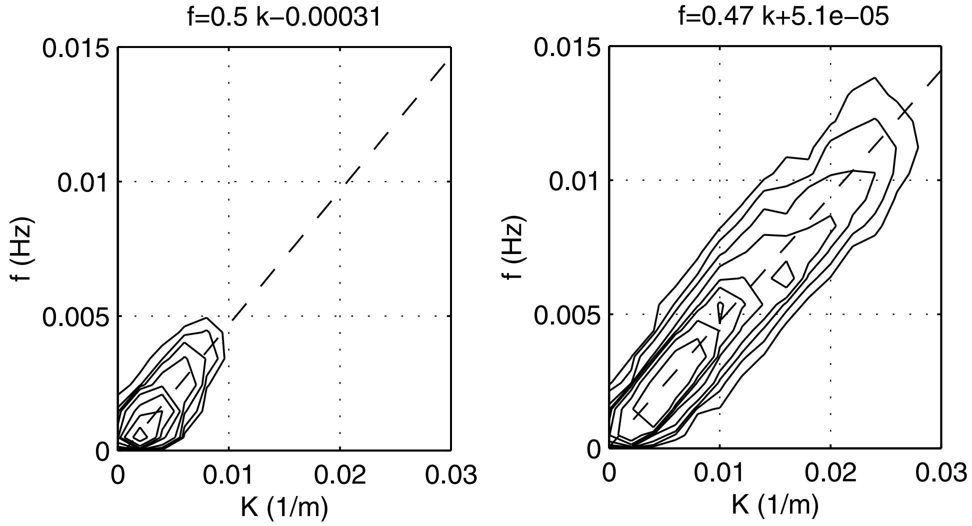

Figure 14. Frequency-longshore wavenumber spectra for $c_f = 0.005$ for shoreline runup computed while (left) neglecting and (right) including wave-current interaction. Contour levels plotted are (10, 20, 40, 80, 160, 320, 640, 1280). The equation for the best-fit dispersion line (dashed line) is noted above each plot.

to shed vortices offshore is also reduced, although probably not eliminated altogether. We find that the time series resulting from simulations with wave-current interaction do not display a tendency towards episodic behavior. In addition, the predicted momentum mixing seaward of the bar crest decreases when wave-current interaction is considered, leading to a longshore current profile that displays a somewhat higher offshore shear but that is otherwise similar.

[46] We note here that previous model simulations excluding wave-current interaction [*Özkan-Haller and Kirby*, 1999] showed that the computed frequency range, energetics and propagation speed of the shear instabilities and the final mean longshore current were in good agreement with observations, but that the tendency for intermittent behavior was overestimated while the offshore shear of the mean longshore current was at times underpredicted. Since *Özkan-Haller and Kirby* [1999] described their flow fields as turbulent shear flows, the results summarized in the above paragraph suggest that the inclusion of wave-current interaction may not alter the prediction of energetics and propagation speed significantly (hence preserving the favorable agreement with data) but may improve data-model comparisons of time series and longshore current shear.

[47] The reduction of the offshore extent of the motions as well as the reduction in their energetics agrees with findings by *Haas et al.* [1999] and *Yu and Slinn* [2003], who observed similar behavior in offshore directed rip currents

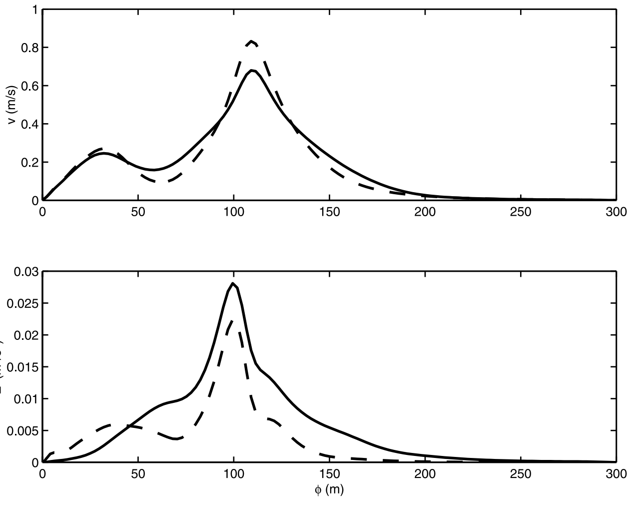

Figure 15. (top) Longshore- and time-averaged longshore current profile and (bottom) turbulent kinetic energy for $c_f = 0.007$ neglecting (solid lines) and including (dashed lines) wave-current interaction.

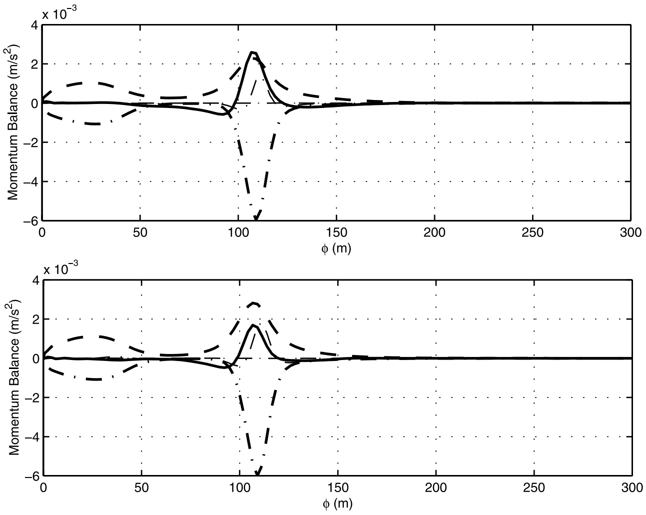

Figure 16. (top) Mean longshore momentum balance neglecting and (bottom) including wave-current interaction for $c_f = 0.007$; $\langle\overline{u(\partial v/\partial x)}\rangle$ (thick solid lines), $-\langle\overline{\tilde{\tau}_y}\rangle$ (thick dash-dotted lines), $-\langle\overline{\tilde{\tau}'_y}\rangle$ (thin dash-dotted lines), $\langle\overline{\tau_{by}}\rangle$ (thick dashed lines), and residual (thin dashed lines).

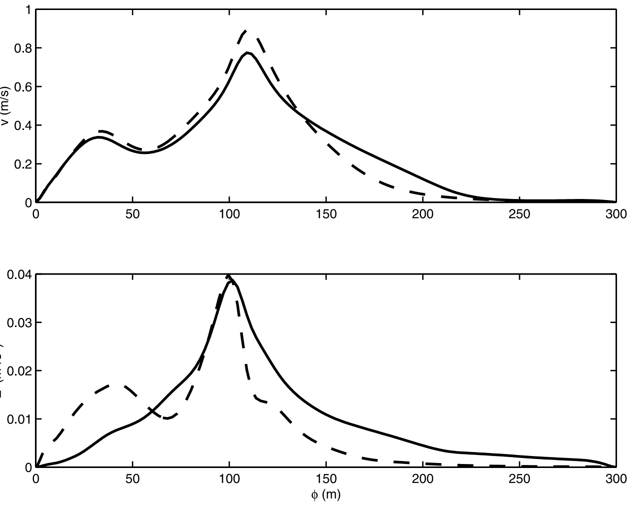

Figure 17. (top) Longshore- and time-averaged longshore current profile and (bottom) turbulent kinetic energy for $c_f = 0.005$ neglecting (solid lines) and including (dashed lines) wave-current interaction.

when wave-current interaction was considered. These effects appear to be related to a transfer of energy from the circulation field to the incident wave field. This can most easily be demonstrated by examining the energy equation for the wave motion (7) [*Yu and Slinn*, 2003]. If we rearrange this equation and isolate the terms related to wave-current interaction on the right-hand side (RHS), we have

$$\frac{\partial E}{\partial t}+\frac{\partial\left(Ec_g\cos\theta\right)}{\partial x'}+\frac{\partial\left(Ec_g\sin\theta\right)}{\partial y'}+\epsilon_b=-\left(\frac{\partial(Eu')}{\partial x'}+\frac{\partial(Ev')}{\partial y'}\right)$$
$$-\left(S_{xx}\frac{\partial u'}{\partial x'}+S_{xy}\left(\frac{\partial u'}{\partial y'}+\frac{\partial v'}{\partial x'}\right)+S_{yy}\frac{\partial v'}{\partial y'}\right). \tag{19}$$

If the RHS of equation (19) is positive, the wave field will gain energy due to work done on the waves by the circulation. We examine the sign and spatial distribution of the RHS in Figure 19 for the case involving wave-current interaction with $c_f = 0.005$.

[48] The vorticity and cross-shore current snapshots in Figure 19 indicate several areas of strong cross-shore currents over the bar crest. Pronounced offshore jets occur at y = 500 and 800 m (neighbored by localized onshore flows immediately downstream). Two weak offshore flow features also occur around y = 100 and 300 m along with strong onshore flow around y = 200 and 400 m. The area of influence of the offshore directed jets at y = 500 and 800 m extends offshore of the bar crest whereas the area of influence of the onshore jets at y = 200 and 400 m extends towards the shoreline into the bar trough. The vorticity snapshot indicates that the longshore current velocities just downstream of the offshore jets are weak.

[49] The RHS of equation (19) displays a pattern that correlates well with the cross-shore gradient of u (correlation coefficient r = 0.87), which demonstrates that the dominant term on the RHS of equation (19) is $-S_{xx}$ $(\partial u'/\partial x')$. In fact, the spatial distribution and magnitude of this term are very similar to the variation of the total RHS displayed in Figure 19c. The areas with a positive sign in Figure 19c indicate that the wave field is gaining energy at the expense of the circulation field, the areas with a negative sign indicate the opposite. The overall effect is the introduction of an asymmetry in the flow. In areas where the current is directed offshore the flow is weakened, while in areas where the current is directed onshore the flow is strengthened. This causes the offshore extent of the flow features to be limited significantly, whereas the shoreward extent of the circulation pattern is not adversely affected by the wave-current interaction process.

[50] Figure 19d shows the instantaneous longshore circulation forcing component $\tilde{\tau}_y$ in equation (1c). In the absence of wave-current interaction, the forcing in the longshore direction is longshore uniform. However, when wave-current interaction is considered, we notice that the areas of strong offshore directed flow (around y = 500 and 800 m) also coincide with areas of stronger than average alongshore forcing. This effect tends to turn the otherwise offshore directed jet by introducing a stronger longshore current component. Immediately downstream of these locations the longshore current forcing is significantly weaker explaining the occurrence of near-zero longshore velocities there. Examining the local angle of wave incidence (Figure 19e) offers an explanation for the longshore variations in the longshore forcing. The presence of the offshore directed currents cause wave focusing and lead to local angles of incidence just upstream of the cross-shore jet that are larger (in absolute value) than the longshore average, leading to an enhanced forcing of the longshore current. Similarly, the local angle of incidence decreases on the downstream side of the offshore directed current leading to weaker forcing at that location.

[51] Our simulations also show that the signature of the instabilities in the shoreline runup is affected significantly by

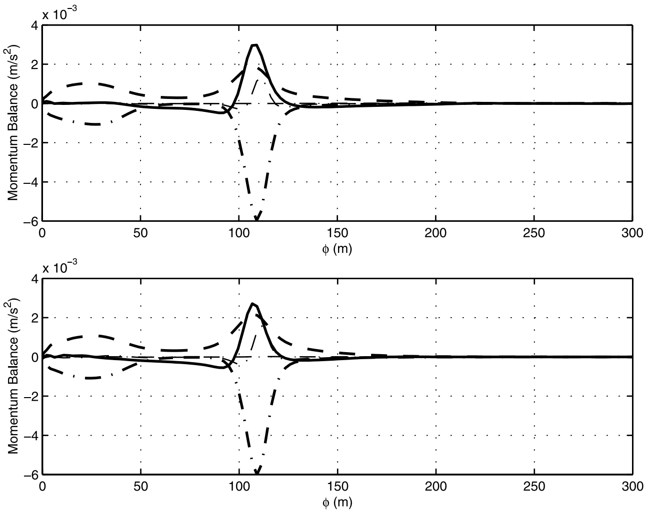

Figure 18. Mean longshore momentum balance (top) neglecting and (bottom) including wave-current interaction for $c_f = 0.005$; $\left\langle\overline{u(\partial v/\partial x)}\right\rangle$ (thick solid lines), $-\left\langle\overline{\tilde{\tau}_y}\right\rangle$ (thick dash-dotted lines), $-\left\langle\overline{\tilde{\tau}'_y}\right\rangle$ (thin dash-dotted lines), $\left\langle\overline{\tau_{by}}\right\rangle$ (thick dashed lines), and residual (thin dashed lines).

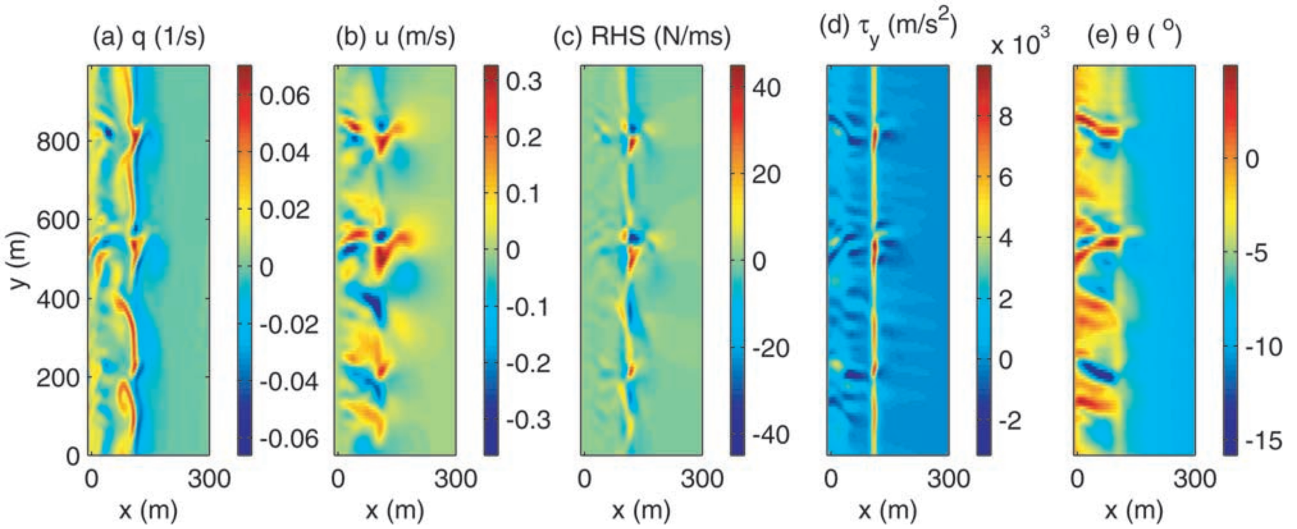

Figure 19. Snapshots at 4.6 hours for $c_f = 0.005$ including wave-current interaction. Snapshots are of the vorticity q (s^{-1}), cross-shore velocity u (m/s), right-hand side of energy equation (19) (N/ms), longshore component of wave forcing $\tilde{\tau}_y$ (m/s^2), and local angle of incidence θ (°).

wave-current interaction processes regardless of the frictional regime. In both frictional regimes that were examined, we found that the energy content and frequency distribution of the shoreline excursions increase when wave-current interaction is considered. These fluctuations near the shoreline have two possible origins: They could be a manifestation of an instability of the main longshore current flowing along the bar crest. Alternately, they could be the result of a separate instability of the shoreline jet. In the latter case, we would expect that the propagation speed of the motions near the shoreline would scale with the shoreline jet peak magnitude, since shear instabilities have previously been shown to propagate at a fraction of the peak current velocity [*Bowen and Holman*, 1989]. However, the simulations indicate that the motions near the shoreline propagate at speeds similar to the undulations near the bar crest (compare Figures 7 and 8). Since the propagation speed of the motions over the bar crest scales with the significantly stronger absolute longshore current peak, this finding suggests that the motions at these two locations may both be closely linked to the instability of the main longshore current peak.

[52] Within this context, it is interesting to note the complicated nature of longshore forcing $\tilde{\tau}_y$ near the shoreline (see Figure 19d). The variations in the forcing are linked to the complicated refraction pattern that is created shoreward of the bar crest. Figure 19e shows that the waves focus significantly around the offshore directed jets. For example, at $y = 500$ m the waves initially focus due to the effect of the strong offshore velocities near the bar crest; however, as the waves propagate further towards shore they encounter a region of onshore directed flow in the bar trough and consequently defocus. Close examination of the wave rays in this region confirms that the individual rays converge and diverge significantly especially shoreward of the bar crest but no ray crossings occur. Since the longshore forcing $\tilde{\tau}_y$ is a function of the local angle of incidence, the repercussion of wave refraction over the circulation field is a complicated forcing pattern which drives a forced circulation field in the bar trough region. Since the cross-shore jets that give rise to this pattern propagate alongshore, so does the forcing pattern and circulation response. It is most likely these alongshore propagating forced vorticity structures that are prominently observed in the shoreline runup signal for both frictional parameters observed herein.

[53] Our findings regarding the strengthened signature of the instabilities in the shoreline runup in the presence of wave-current interaction are especially relevant in light of the laboratory experiments of *Reniers et al.* [1997], who stated that they could visually observe modification of the wave crests especially near the shoreline after the initiation of shear waves in a laboratory basin. The wave-current interaction process may also help explain the surprisingly energetic signature of a shear instability in field observations of shoreline runup by *Holland and Holman* [1999].

[54] The longshore current profiles for both friction factors display higher peak values when wave-current interaction is considered. Examination of the mean longshore momentum balance also confirms that less momentum mixing is caused by the instabilities when wave-current interaction is accounted for. This is related to two reasons: the reduced energy content of the fluctuations (as seen in Figure 15) and the more regular nature of the instabilities (in which case the phase relationship between the longshore and cross-shore components of the velocities leads to less mixing). The occurrence of a higher longshore current peak and the increased propagation speed of the fluctuations when wave-current interaction is considered are also likely to be closely linked, since the propagation speed scales with the longshore current peak. Furthermore, the reduced amplitude of the cross-shore velocity that is especially apparent for $c_f = 0.007$ also helps explain the increased propagation speed, since shear instabilities propagate faster for lower nonlinearity [*Allen et al.*, 1996].

[55] We are currently investigating the linear instability characteristics of the combined wave-current system studied here to isolate the reasons behind the delayed onset of the instabilities when wave-current interaction is considered. The analysis involves a system of seven coupled differential

equations and the solution for unstable modes of behavior is complicated by the occurrence of spurious modes in the numerical solution procedure. Such a complication was also experienced by *Falqués and Iranzo* [1994] while examining a three-equation system. We hope to present the results of this study in a separate publication at a later date.

[56] In order to isolate the reasons for the diminished effect of the wave-current interaction terms for low frictional damping, we have analyzed the size of the terms on the RHS of equation (19) for the two cases involving different frictional coefficients since the RHS of equation (19) gives an indication of the amount of work that is performed by the circulation field on the incident waves. It turns out that the size of these terms is similar for both frictional conditions analyzed herein suggesting that the circulation field is utilizing a similar amount of energy to modify the wave field for either case. This may seem counterintuitive at first since the amplitudes of the cross-shore jets are higher when the friction coefficient is low, and therefore the effect of these higher offshore currents on the waves should be more profound. However, their offshore extent is also larger for lower friction resulting in a cross-shore gradient of u that is similar in magnitude for both frictional values. Since the RHS of equation (19) is proportional to this cross-shore gradient, $(\partial u/\partial x)$ provides a good proxy for the amount of work the circulation field performs on the wave field. Therefore, the similarity of the values of $(\partial u/\partial x)$ for both cases indicates that the amount of energy extracted from the current field in favor of the wave field is similar in both cases. However, the amount of energy available is significantly higher for the low friction case (c_f = 0.005). Hence, the relative energy loss is less for lower friction; therefore, the effects are less pronounced. Another finding that supports this idea concerns the mean turbulent kinetic energy. We find that the cross-shore mean of the averaged turbulent kinetic energy E' (Figures 15 and 17) decreases by the same amount (about 0.002 $\mathrm{m}^2\ \mathrm{s}^2$) when wave-current interaction is considered for both c_f = 0.007 and 0.005, although the amount of available E' for c_f = 0.005 is larger by a factor of 2 compared to c_f = 0.007.

[57] It is worthwhile to reiterate at this point that the energy and wavenumber equations (7) and (10) do not account for the effects of wave diffraction due to the presence of the currents. Diffraction effects will be important in situations where the curvature of the wave height becomes significant. This often occurs near areas where wave propagation is locally blocked or where wave rays are so strongly bent that they cross or nearly cross, generating a short-crested wave pattern. A nondimensional parameter that helps assess the importance of wave diffraction for a given situation is a factor defined by *Battjes* [1968] as

$$\delta = \frac{1}{k^2}\frac{1}{H}\left(\frac{\partial^2 H}{\partial x^2} + \frac{\partial^2 H}{\partial y^2}\right). \tag{20}$$

Physically, this factor represents the normalized difference between the group velocity of the incident waves and the group velocity computed while neglecting diffraction. Therefore, if δ is a small parameter, diffraction effects can be considered to be small. In all of our simulations we find that $|\delta| < 0.05$ for the majority of the modeling domain and reaches ~0.2 for a small region of the domain in the immediate vicinity of the bar crest (90 m < x < 120 m).

[58] Finally, it is noted that the changes in the absolute frequency found herein are in general only a minor repercussion of the modeling of wave refraction since the variations only cause temporal changes in the wave period of a few percent. Although the possible occurrence of variations in the absolute frequency was recognized early on by *Whitham* [1974, p. 383], the present simulations suggest that the variations in the peak wave period due to the mechanisms analyzed herein would be very minor. Even if small temporal variations of the wave period were detectable in field measurements, it would be difficult, if not impossible, to conclusively link such variations to temporal variations in the circulation or bathymetry, since any observed frequency variations could easily be accounted for by natural shifts in the peak frequency in time due to the nature of a particular storm.

[59] The noted small variations in the wave frequency suggest that the accelerations in the circulation field do not affect the results significantly. Hence, assuming that the wave field adjusts instantaneously to any changes in the circulation field and updating the wave field periodically would likely be adequate in the cases studied herein. However, it is noted that the wave model used herein has wider applicability and can further be utilized in situations where a temporal variation of the offshore wave energy is present, either due to transients caused by an approaching storm or due to wave grouping.

Appendix A: Synthetic Tests of the Wave-Current Interaction Model

[60] In this section we present two example cases demonstrating how the wave field responds to temporal variations in its environment. In a situation where the wave field is explicitly allowed to vary in time, the wave period may no longer remain a constant. This property is best demonstrated by focusing on the kinematics of the waves for a simple case involving no current velocities or setup, but a temporally varying bottom. Therefore, our first test case involves a constant depth channel with a bump growing over time at the center of the channel. Our second case is more applicable to the study if shear instabilities and involves the imposition of an ambient offshore directed current. We analyze the response of the wave field to an acceleration in the current.

A1. Growth of a Bump in Constant Depth

[61] In this case, we artificially suppress the generation of any circulation or wave-induced setup and concentrate on the kinematics of a wave field propagating over a slowly growing bump in an otherwise constant-depth channel. In this case, the dispersion relationship collapses to

$$\omega^2 = gk \tanh kh. \tag{A1}$$

Considering only one horizontal dimension, the conservation of waves equation (10) collapses into

$$\frac{\partial k}{\partial t} + \frac{\partial \omega}{\partial x'} = 0 \quad \text{or} \quad \frac{\partial k}{\partial t} - \frac{\partial \omega}{\partial x} = 0. \tag{A2}$$

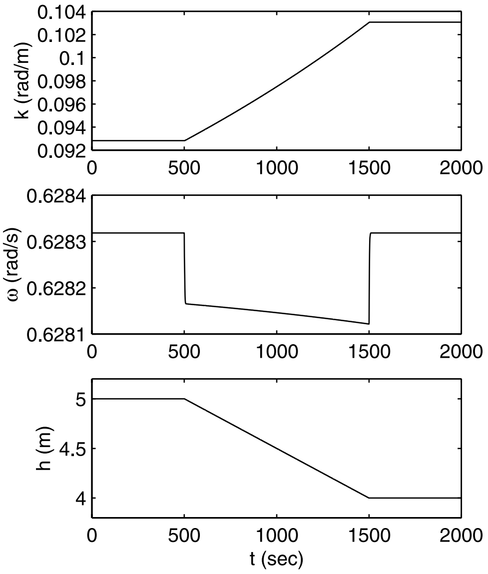

Figure A1. Time series of wavenumber k, absolute frequency ω, and water depth h sampled at x = 100 m.

If the water depth h varies spatially, ω remains a constant and equation (A1) dictates that k varies in space to account for changes in the water depth. In a situation where h varies temporally, it follows from equation (A1) that k must vary temporally. In this case, equation (A2) dictates that ω must vary spatially [*Whitham*, 1974].

[62] Figure A1 depicts the temporal response of the wave field in response to a bump growing at the bottom of an otherwise constant-depth channel. The incident waves occur at 0.1 Hz and propagate in the $-x$-direction. The bump grows to 1 m height in the course of 1000 s. The first 500 s of the simulation the water depth is kept constant and, as expected, the wavenumber and frequency of the waves also remain constant. The time series of the water depth displays a piece-wise smooth character with a discontinuity in $(\partial h/\partial t)$ at $t = 500$ s, when the linear growth of the water depth is introduced, and at t = 1500 s when the growth of the bump ceases. The wavenumber displays a similar character; however, the temporal variation of the wavenumber results in a curve that is slightly concave upward instead of being linear, hence $(\partial k/\partial t)$ increases slightly with time. The frequency displays a jump discontinuity at t = 500 and 1500 s coincident with the abrupt introduction and cessation of a temporal gradient in h. The jump discontinuities in ω are a direct consequence of the slope discontinuities in k, since equation (A2) dictates that $(\partial\omega/\partial x)$ has to be non-zero when $(\partial k/\partial t)$ is introduced. For $500s < t < 1000s$, ω displays a slight decrease which is linked to the small increase in $(\partial k/\partial t)$ over this period of time.

[63] Snapshots of the wavenumber, frequency and water depth (Figure A2) show a local change in the wavenumber corresponding to the local change in the water depth. The location of the maximum spatial gradient in the frequency corresponds to the location of the maximum temporal change in the value of the wavenumber (x = 100 m). In regions close to x = 0 and 200 m, where temporal variation in the water depth is absent, the frequency is a constant. It locally displays spatial variation during the period of time that h varies, but subsequently returns to its original value.

[64] The magnitude of change in the wave frequency in this example is minimal although a 20% change in the water depth and 10% change in the wavelength is present. Further simulations show that the magnitude of the change in the frequency is proportional to the time rate of change of the wavenumber. In other words, if the wavenumber varies rapidly in time the change in frequency is more pronounced.

A2. Temporally Varying Offshore Directed Current on a Barred Beach

[65] A more realistic example results from the consideration of an offshore directed current on a barred beach. The water depth h is given by equation (16), and 10-s waves propagate in the $-x$-direction. We artificially impose an ambient offshore directed current centered over the bar crest that ramps up to a maximum of 0.3 m/s within a 100-s time frame. The width and offshore extent of the current are chosen to mimic the properties of offshore directed currents resulting from the simulations of shear instabilities of the longshore current. The spatial distribution of the current u and the water depth h are depicted in Figure A3. The acceleration of the current is equivalent to those observed in the simulations of the shear instabilities and is much more rapid than the temporal variation introduced in the previous example.

[66] Time series of several variables at the location of the peak current are shown in Figure A4. To avoid jump discontinuities in the absolute frequency, the temporal variation of the current amplitude is imposed such that its first derivative is smooth. The cross-shore wavenumber component displays a 10% variation due to the effect of

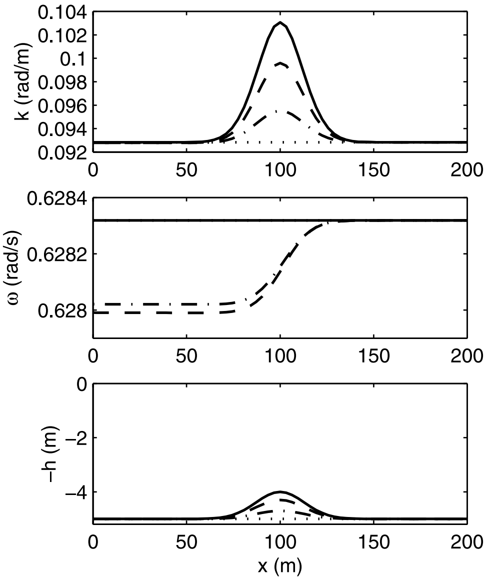

Figure A2. Snapshots of wavenumber k, absolute frequency ω, and negative water depth h at t = 400 (dotted), 800 (dash-dotted), 1200 (dashed) and 1600 s (solid). The dotted line in the middle panel coincides with the solid line.

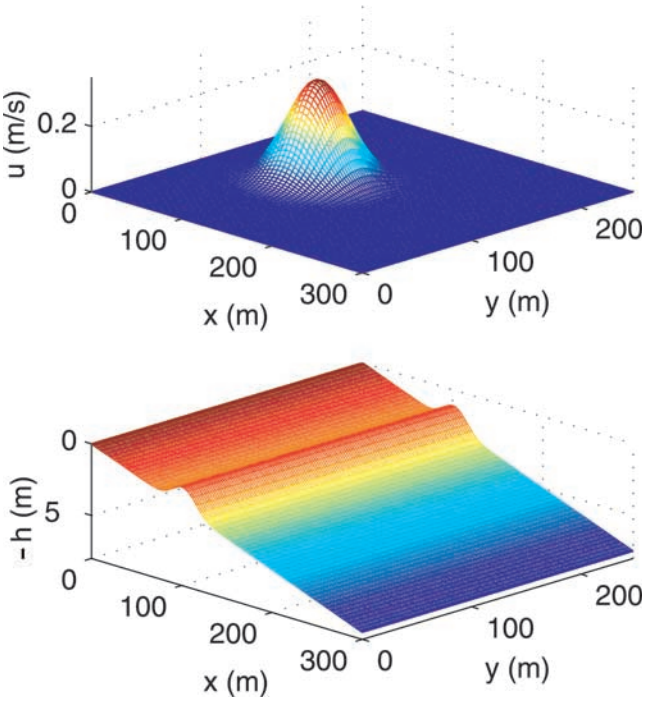

Figure A3. (top) Ambient current u and (bottom) negative water depth $-h$.

the opposing current. The longshore wavenumber component displays minimal variation; however, the longshore location at which this time series is collected corresponds to the location of the current maximum, and the effect of the opposing current on the longshore wavenumber is minimal at this location. The refraction effect is most pronounced to the right and left of the current maximum where the wave rays are significantly bent (see Figure A5). The local wave angle $\theta(=\arctan(k_y/k_x))$ varies by 100% over the bar crest, and the longshore variation reaches a maximum in the bar trough region where local wave angles range from $-14°$ to $4°$ (not shown). The resulting wave crests (Figure A6) can be observed to be significantly affected by the presence of the current.

[67] Snapshots of the variation in the absolute frequency are shown in Figure A7 and reveal that the variation in the wave period exceeds 2% of its original value during the period of time where significant flow acceleration is experienced. Substituting the dispersion relationship into the conservation of wavenumber equations (10) reveals that the behavior of the absolute frequency is governed by a wave equation. Hence, it should come as no surprise that the initial disturbance to the constant frequency field caused by spatially localized accelerations propagates towards the shoreline at an angle that corresponds to the small local angle of wave incidence. When the flow accelerations cease to exist, the remaining disturbance leaves the domain of interest through the shoreline boundary and the frequency field returns to its original constant state.

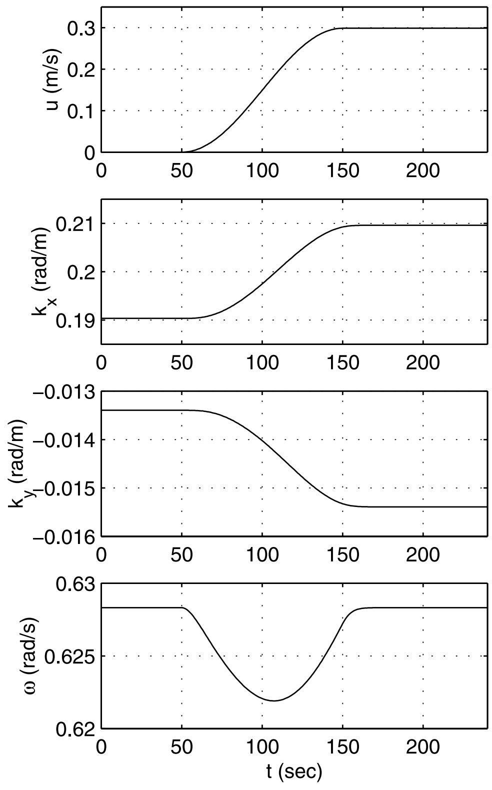

Figure A4. Time series of offshore current u, cross-shore wavenumber component k_x, longshore wavenumber component k_y, and absolute frequency ω at $(x, y) = (100$ m, 125 m).

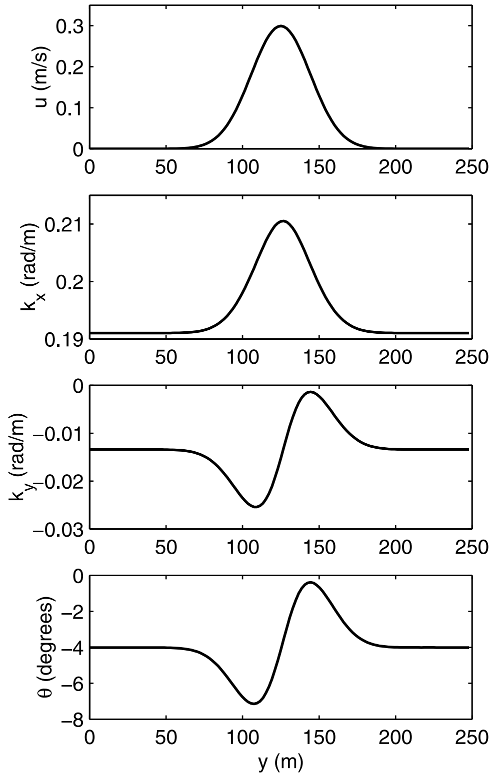

Figure A5. Alongshore variation of the current u, cross-shore wavenumber component k_x, longshore wavenumber component k_y, and local angle of incidence θ on the bar crest at $x = 100$ m.

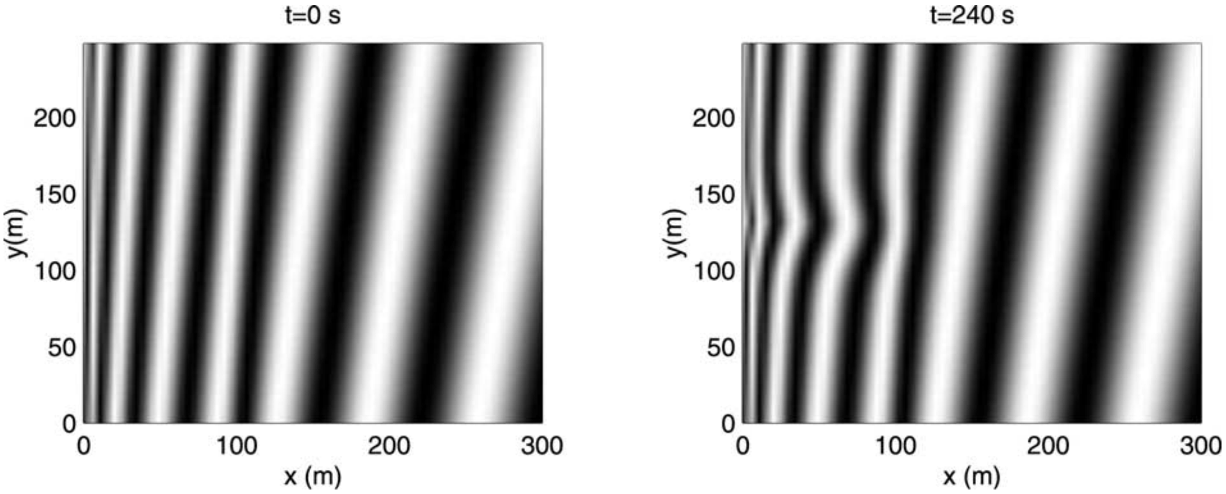

Figure A6. Snapshots the wave form at t = 0, and 240 s. The light (dark) regions indicate wave crests (troughs).

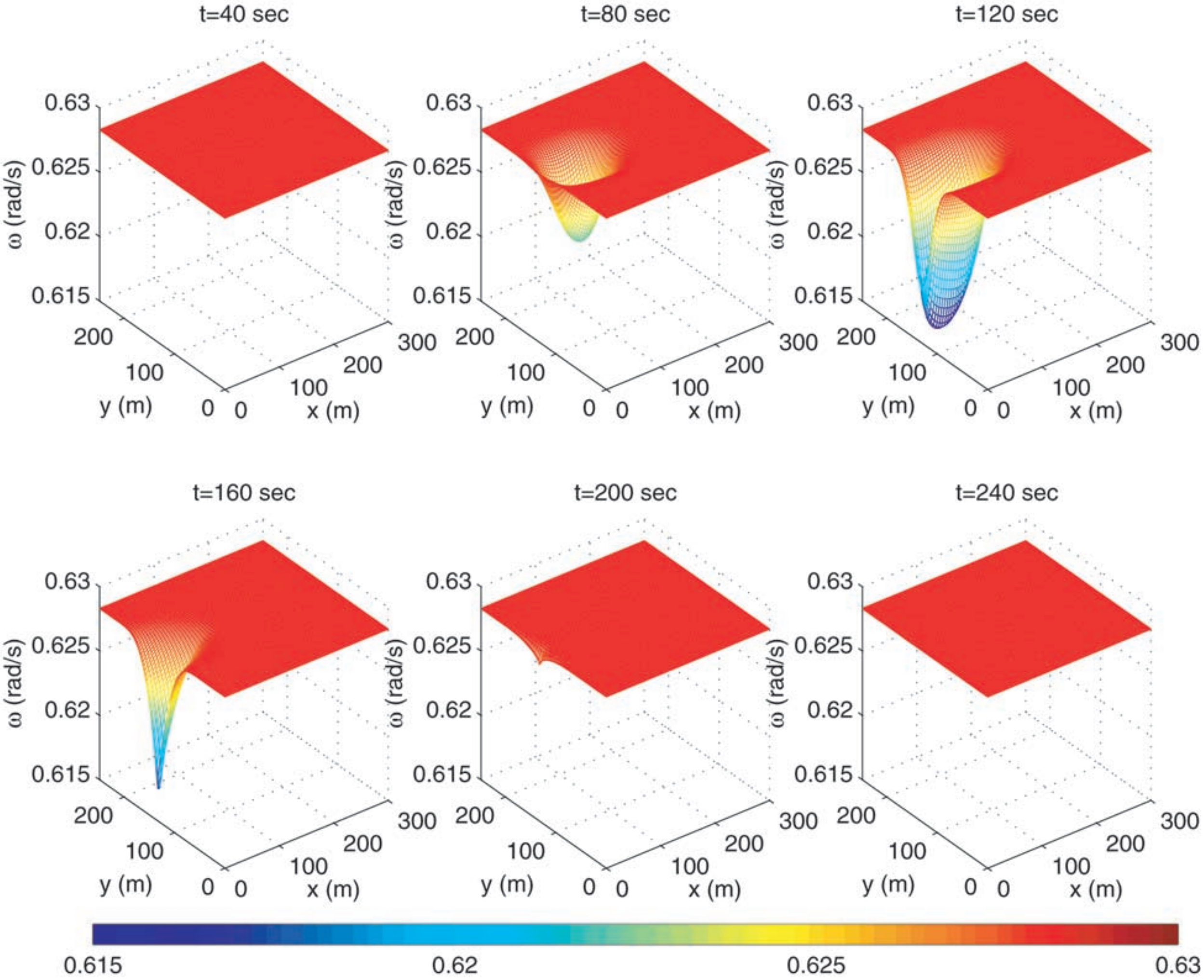

Figure A7. Snapshots of absolute frequency ω at t = 40, 80, 120, 160, 200 and 240 s.

[68] **Acknowledgments.** We gratefully acknowledge two anonymous reviewers whose comments helped improve the paper. Many thanks to Merrick Haller who also provided many useful comments. Funding for this work has been provided by the Office of Naval Research Young Investigator Program under grant N00014-99-1-0490 at the University of Michigan and N00014-02-1-0069 at the Oregon State University.

References

Allen, J. S., P. A. Newberger, and R. A. Holman, Nonlinear shear instabilities of alongshore currents on plane beaches, *J. Fluid Mech.*, *310*, 181–213, 1996.

Battjes, J., Refraction of water waves, *J. Waterw. Harbors Coastal Eng. Div. Am. Soc. Civ. Eng.*, *94*, 437–451, 1968.

Battjes, J., Modeling of turbulence in the surf zone, in *Symposium on Modeling Techniques: Second Annual Symposium of the Waterways, Harbors, and Coastal Engineering Division of ASCE*, vol. 2, pp. 1050–1061, Am. Soc. of Civ. Eng., New York, 1975.

Bowen, A. J., and R. A. Holman, Shear instabilities of the mean longshore current: 1. Theory, *J. Geophys. Res.*, *94*, 18,023–18,030, 1989.

Brocchini, M., and D. H. Peregrine, Integral flow properties of the swash zone and averaging, *J. Fluid Mech.*, *317*, 241–273, 1996.

Chen, Q., R. A. Dalrymple, J. T. Kirby, A. B. Kennedy, and M. C. Haller, Boussinesq modeling of a rip current system, *J. Geophys. Res.*, *104*, 20,617–20,637, 1999.

Dean, R. G., and R. A. Dalrymple, *Water Wave Mechanics for Engineers and Scientists*, World Sci., River Edge, N. J., 1991.

Dodd, N., V. Iranzo, and A. Reniers, Shear instabilities of wave-driven alongshore currents, *Rev. Geophys.*, *38*, 437–463, 2000.

Falqués, A., and V. Iranzo, Numerical simulation of vorticity waves in the nearshore, *J. Geophys. Res.*, *99*, 825–841, 1994.

Haas, K. A., I. A. Svendsen, and M. C. Haller, Numerical modeling of nearshore circulation on a barred beach with rip channels, in *Coastal Engineering 1998: Proceedings of the 26th International Conference*, vol. 1, edited by B. L. Edge, pp. 801–814, Am. Soc. of Civ. Eng., New York, 1999.

Holland, K. T., and R. A. Holman, Wavenumber-frequency structure of infragravity swash motions, *J. Geophys. Res.*, *104*, 13,479–13,488, 1999.

Longuet-Higgins, M. S., and R. W. Stewart, Radiation stress in water waves, a physical discussion with application, *Deep Sea Res.*, *11*, 529–563, 1964.

Madsen, P. A., O. R. Sorensen, and H. A. Schäffer, Surf zone dynamics simulated by a Boussinesq-type model: I. Model description and cross-shore motion of regular waves, *Coastal Eng.*, *32*, 255–287, 1997.

Mei, C. C., *The Applied Dynamics of Ocean Surface Waves*, World Sci., River Edge, N. J., 1990.

Nakamura, S., and N. Dodd, Observation and simulation of low-frequency waves on two natural beaches, in *Coastal Engineering 1998: Proceedings of the 26th International Conference*, vol. 2, edited by B. L. Edge, pp. 1313–1322, Am. Soc. of Civ. Eng., New York, 1999.

Oltman-Shay, J., P. A. Howd, and W. A. Birkemeier, Shear instabilities of the mean longshore current: 2. Field observations, *J. Geophys. Res.*, *94*, 18,031–18,042, 1989.

Özkan-Haller, H. T., and J. T. Kirby, A Fourier-Chebyshev collocation method for the shallow water equations including shoreline runup, *Appl. Ocean Res.*, *19*, 21–34, 1997.

Özkan-Haller, H. T., and J. T. Kirby, Nonlinear evolution of shear instabilities of the longshore current: A comparison of observations and computations, *J. Geophys. Res.*, *104*, 25,953–25,984, 1999.

Park, K.-Y., and A. G. L. Borthwick, Quadtree grid numerical model of nearshore wave-current interaction, *Coastal Eng.*, *42*, 219–239, 2001.

Phillips, O. M., *The Dynamics of the Upper Ocean*, Cambridge Univ. Press, New York, 1982.

Reniers, A. J. H. M., J. A. Battjes, A. Falqués, and D. A. Huntley, A laboratory study on the shear instability of longshore currents, *J. Geophys. Res.*, *102*, 8597–8609, 1997.

Slinn, D. N., J. S. Allen, P. A. Newberger, and R. A. Holman, Nonlinear shear instabilities of alongshore currents over barred beaches, *J. Geophys. Res.*, *103*, 18,357–18,379, 1998.

Thornton, E. B., and R. T. Guza, Transformation of wave height distribution, *J. Geophys. Res.*, *88*, 5925–5938, 1983.

Whitham, G. B., *Linear and Nonlinear Waves*, John Wiley, New York, 1974.

Yoo, D., and B. A. O'Conner, Diffraction of waves in caustics, *J. Waterw. Port Coastal Ocean Eng.*, *114*, 715–730, 1988.

Yu J., and D. N. Slinn, Effects of wave-current interaction on rip currents, *J. Geophys. Res.*, *108*, 3088, doi:10.1029/2001JC001105, 2003.

H. T. Özkan-Haller, College of Oceanic and Atmospheric Sciences, Oregon State University, 104 Ocean Administration Building, Corvallis, OR 97331-5503, USA. (ozkan@coas.oregonstate.edu)

Y. Li, Department of Naval Architecture and Marine Engineering, University of Michigan, 2600 Draper Road, Ann Arbor, MI 48109-2145, USA. (yel@engin.umich.edu)